APL Materials

Ellingham diagrams of binary oxides

Shun-Li Shang ✉ 📷 ; Shuang Lin 📷 ; Michael C. Gao 📷 ; Darrell G. Schlom 📷 ; Zi-Kui Liu 📷
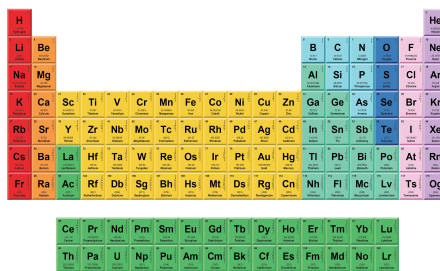
Check for updates

View Online   Export Citation

Ellingham diagrams of binary oxides

View Online   Export Citation   CrossMark

Shun-Li Shang,[1,2,a] (ID) **Shuang Lin,**[1] (ID) **Michael C. Gao,**[2] (ID) **Darrell G. Schlom,**[3,4,5] (ID) **and Zi-Kui Liu**[1] (ID)

AFFILIATIONS

[1] Department of Materials Science and Engineering, The Pennsylvania State University, University Park, Pennsylvania 16802, USA
[2] Materials Engineering and Manufacturing Directorate, National Energy Technology Laboratory, Albany, Oregon 97321, USA
[3] Department of Materials Science and Engineering, Cornell University, Ithaca, New York 14853, USA
[4] Kavli Institute at Cornell for Nanoscale Science, Ithaca, New York 14853, USA
[5] Leibniz-Institut für Kristallzüchtung, Max-Born-Str. 2, 12489 Berlin, Germany

[a] Author to whom correspondence should be addressed: sus26@psu.edu

ABSTRACT

Controlling the oxidation state of constituents by tuning the oxidizing environment and materials chemistry is vital to the successful synthesis of targeted binary or multicomponent oxides. We have conducted a comprehensive thermodynamic analysis of 137 binary oxides to calculate their Ellingham diagrams. It is found that the "reactive" elements that oxidize easily are the f-block elements (lanthanides and actinides), elements in groups II, III, and IV (alkaline earth, Sc, Y, Ti, Zr, and Hf), and Al and Li. In contrast, the "noble" elements are easily reduced. These are coinage metals (Cu, Ag, and especially Au), Pt-group elements, and Hg and Se. Machine learning-based sequential feature selection indicates that the ease of oxidation can be represented by the electronic structures of pure elements, for example, their d- and s-valence electrons, Mendeleev numbers, and groups, making the Periodic Table a useful tool for qualitatively assessing the ease of oxidation. The other elemental features that weakly correlate with the ease of oxidation are thermochemical properties such as melting points and the standard entropy at 298 K of pure elements. Applying Ellingham diagrams enables the oxidation of multicomponent materials to be predicted, such as the Fe–20Cr–20Ni alloy (in wt. %) and the equimolar high entropy alloy of AlCoCrFeNi. These Ellingham diagram-based predictions are in accordance with thermodynamic calculations using the CALPHAD approach and experimental observations in the literature.

I. INTRODUCTION

Oxides are of enormous interest for a wide range of applications due to their broad range of extraordinary, unique properties.[1] For example, a dense, stable, and continuous scale (e.g., α-Al$_2$O$_3$, α-Cr$_2$O$_3$, SiO$_2$,[2] and CrTaO$_4$[3]) formed on base alloys provides both oxidation and hot corrosion protection. (Multi)functional oxides garner enormous interest, including the metal PdCoO$_2$;[4] the ferroelectric Pb(Zr,Ti)O$_3$;[5] the ferromagnets La$_{0.7}$Sr$_{0.3}$MnO$_3$[6] and Sr$_2$FeMoO$_6$;[7] the multiferroics BiFeO$_3$[8] and BiMnO$_3$;[9] the high-temperature superconductor HgBa$_2$Ca$_2$Cu$_3$O$_{1+x}$;[10] the topological insulator Sr$_3$SnO;[11] and the catalysts and electrocatalysts LaMnO$_{3+\delta}$ and LaNiO$_3$,[12] Ba$_{0.5}$Sr$_{0.5}$Co$_{0.8}$Fe$_{0.2}$O$_{3-\delta}$,[13] and SrIrO$_3$.[14] Synthesizing desired oxides is often challenging, particularly when multivalent cations are involved. For example, the oxidation conditions needed to form Mo^{2+} (say in SrMoO$_3$, a conductive oxide with conductivity comparable to platinum)[15] are far less oxidizing than what is needed to form Mo^{6+} (say in SrMoO$_4$, an unwanted insulating impurity phase commonly seen in the attempted synthesis of SrMoO$_3$).[16] Controlling the oxidation state of constituents is, hence, fundamental for material synthesis[17] as well as material degradation.[2]

The relative stability of desired as well as undesired oxides can be examined by the Ellingham diagram, which was introduced by Ellingham in 1944[18] to plot the change in the standard Gibbs energy (ΔG^o) vs temperature (T) for a given reaction; see details in Sec. II A. In the context of oxidation, the Ellingham diagram determines the relative ease of reducing a given oxide to element(s) or another oxide(s), i.e., the lower the line on the Ellingham diagram, the more thermodynamically stable the oxide relative to the other oxides, where the "noble" metals (or elements, or oxides) are closer to the top of the diagram and the "reactive" metals are closer to the bottom of the diagram. In addition, replacing ΔG^o with the partial pressure of oxygen, P_{O_2} (see Sec. II A), the Ellingham diagram gives

the equilibrium P_{O_2} values for a given reaction as a function of T, where the element (or oxide) will be oxidized at higher P_{O_2} values or will be reduced at lower P_{O_2} values. The Ellingham diagram is, hence, a useful tool to understand the relative stability of oxides. For example, Ellingham diagrams are often used to guide the growth of oxide thin films by molecular-beam epitaxy (MBE), including high-temperature superconductors[19,20] as well as the adsorption-controlled growths of $BaSnO_3$,[21] $BiFeO_3$,[22] $BiMnO_3$,[9] $LuFe_2O_4$,[23] $PbTiO_3$,[24] $SrRuO_3$ and $CaRuO_3$,[25] and Sr_3SnO.[11] Ellingham diagrams have also been used to understand the thermodynamic stability of the spinel $MgAl_2O_4$ under strong reducing conditions,[26] the structural phase transition of $Pr_2NiO_{4+\delta}$ involving variation of oxygen content,[27] the hot isostatic press processes,[28] and the oxidation behaviors of transition metals,[29] ultrahigh-entropy ceramics,[30] and multi-principal component materials.[31,32]

Despite their importance, a comprehensive compilation of oxide Ellingham diagrams is not present in the literature. For instance, Backman and Opila[31] calculated the Ellingham diagrams for groups IV, V, and VI binary oxides using the FactSage software and the Fact Pure Substance database.[33] Birks et al.,[34] Ellingham,[18] Gleeson,[35] and Smeltzer and Young[29] reported the selected Ellingham diagrams, which are mainly for transitional metal binary oxides.

This work aims to enrich the literature by providing, first, a compilation of Ellingham diagrams for 137 binary oxides based on a comprehensive thermodynamic analysis. Next, the ease of oxidation as indicated by Ellingham diagrams is examined through machine learning (ML) based correlation analysis in terms of the fundamental properties of pure elements. As an example of their utility, the thermodynamic stabilities of the Fe–20Cr–20Ni alloy (in wt. %) and the equimolar high entropy alloy AlCoCrFeNi in oxidizing environments are predicted using the CALPHAD (calculations of phase diagram) approach[36] in terms of the calculated Ellingham diagrams. It is anticipated that the presently predicted Ellingham diagrams establish the growth conditions of many oxides, enabling a quick survey of their growth conditions by considering the maximum oxygen partial pressure that can be provided in a given synthesis method.

II. METHODOLOGY

A. Basis of Ellingham diagram

In 1944, Ellingham[18] introduced a diagram that now bears his name to study metallurgic processes involving oxides and sulfides. This diagram shows the change in the standard Gibbs energy (ΔG^o) with respect to temperature (T) for a given reaction. It is a measure of the thermodynamic driving force that makes a reaction occur. In the present work, the following two scenarios are considered to form binary oxides, where the reactions in "scenario one" are from metal/element M to oxide M_xO_y,

$$\frac{2x}{y} M(s \text{ or } l) + O_2(g) = \frac{2}{y} M_xO_y(s \text{ or } l), \quad (1)$$
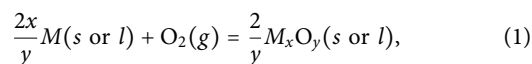
and the reactions in "scenario two" are from one oxide, M_aO_b, to another oxide, M_xO_y,

$$\frac{2x}{ay - bx} M_aO_b(s \text{ or } l) + O_2(g) = \frac{2a}{ay - bx} M_xO_y(s \text{ or } l). \quad (2)$$
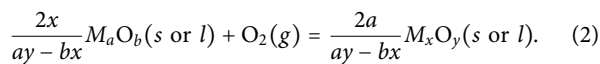
Here, the letters s, l, and g indicate the solid, liquid, and gas phases, respectively. Note that (i) $ay > bx$ in Eq. (2), indicating that the oxidation process is from M_aO_b to M_xO_y; (ii) the oxygen gas species O_2 is selected due to its dominance in comparison with the other species of O_1 and O_3;[37] and (iii) the reactions are under the total pressure (P_{tot}) of one atmosphere (atm) by consuming one mole of oxygen (O_2). Assuming the activities of liquids and solids as unity, the T-dependent equilibrium constant K for Eqs. (1) and (2) is determined by the activity of oxygen (a_{O_2}),[35]

$$K = 1/a_{O_2}. \quad (3)$$

For the reactions in Eqs. (1) and (2), the Gibbs energy change under isobaric conditions (e.g., at 1 atm) is given by

$$\Delta G = \Delta G^o + RT \ln K = \Delta G^o - RT \ln a_{O_2}, \quad (4)$$

where ΔG^o is the standard Gibbs energy of formation for Eqs. (1) and (2) at absolute temperature T, and R is the gas constant. Equation (4) indicates that if $\Delta G < 0$, the reaction can proceed spontaneously, and if $\Delta G > 0$, the reaction is thermodynamically unfavorable. At equilibrium ($\Delta G = 0$), the reaction is at equilibrium, and

$$\Delta G^o = RT \ln a_{O_2}. \quad (5)$$

In the present work, we set the reference pressure $P_{ref} = P_{tot} = 1$ atm(10^5 Pa), and the unit of P_{O_2} is Torr. If oxygen behaves ideally,

$$a_{O_2} = \frac{P_{O_2}}{P_{ref}} = \frac{133.33 P_{O_2}}{10^5}, \quad (6)$$

showing that $P_{O_2} = 750 a_{O_2}$ Torr. Note that $\Delta G^o = \Delta H^o - T\Delta S^o$, where ΔH^o and ΔS^o are the change in the standard enthalpy and the change in the standard entropy of the reaction, respectively. When ΔH^o and ΔS^o are essentially constant with respect to temperature, the ΔG^o vs T plots are the straight lines, with ΔS^o being the slope [i.e., the molar entropy of oxygen since $\Delta S^o \cong -S_{O_2}^o$,[35] for Eqs. (1) and (2)] and ΔH^o being the intercept.

It is worth mentioning that the ΔG^o vs T plot is usually called an Ellingham diagram,[18] while the ln K vs $1/T$ plot is usually called the van't Hoff diagram, and they are equivalent.[38] In the present work, the "P_{O_2} vs $1/T$" plot is adopted as the Ellingham P–T phase diagram to facilitate the determination of P_{O_2} for a given reaction—the same as our previous applications for guiding the MBE growth of oxides.[9,11,19–25]

B. Thermodynamic calculation of Ellingham diagram

An Ellingham diagram involves the determination of ΔG^o or P_{O_2} with respect to T for a given reaction. In the present work, these thermodynamic calculations were performed by the Thermo-Calc software[39] using the SGTE substance database (i.e., the SSUB5).[40] The missing thermodynamic properties for the Pt–O compounds (PtO, PtO_2, and Pt_3O_4) were added to SSUB5 using the reported enthalpies and entropies of formation at room temperature.[41] Thermodynamic calculations of ΔG^o or P_{O_2} can use one of the following three methods:

- Method **I** is a direct calculation of ΔG^o of a reaction of interest, where P_{O_2} is determined by Eqs. (5) and (6). In this case,

tabulated ΔG^o values can be predicted, where only the gas species of O_2 is included in the calculations and all the other gas species are excluded.

- Method **II (Eq-reaction)** is an equilibrium calculation considering all phases relevant to the reaction of interest. In this case, all gas species (e.g., O_1, O_2, O_3, and simple and complex M and M–O species) are considered, and the P_{O_2} values are determined following thermodynamic calculations. In the present work, method II is primarily used due to its high-throughput advantage for the calculations.

- Method **III (Eq-system)** is an equilibrium calculation considering all available phases in the system of interest (e.g., the Fe–O system), and the Ellingham diagrams for all reactions in this system are calculated simultaneously. Method III is, in fact, the equilibrium calculations of the P–T phase diagram for a given system; see our previous calculations for ternary oxides of $BaSnO_3$,[21] $BiFeO_3$,[22] $BiMnO_3$,[9] $LuFe_2O_4$,[23] $PbTiO_3$,[24] $SrRuO_3$ and $CaRuO_3$,[25] and Sr_3SnO.[11] Importantly, nonstable oxides are excluded from method III, and successful calculations are not easy for some systems due in part to the care needed in selecting initial conditions. We use the term "nonstable phase" to denote that this phase is absent in the temperature-composition phase diagram at ambient pressure, and we do not know whether this phase possesses imaginary phonon modes or not, i.e., whether they are metastable or unstable.

In principle, all three of the above methods predict the same Ellingham diagrams (see Sec. III A, where the Fe–O Ellingham diagrams are predicted by both methods II and III). During our calculations of Ellingham diagrams using method II, the following two situations are considered: First, only oxides that appear at some temperatures in the phase diagram at 1 atm are included. This is achieved by examining the calculated phase diagrams. To appear in a phase diagram, the oxide must be stable at that T and P_{O_2}, but in our analysis, we consider such oxides even at temperatures where they are no longer stable, i.e., they are metastable. Meanwhile,

nonstable oxides identified by thermodynamic calculations are excluded (except for the nonstable Au_2O_3, which is the only Au-based binary oxide in SSUB5). A total of 137 binary oxides are considered to build the set of Ellingham diagrams from the 155 oxides available in the SSUB5 database; they are given in the Excel file of the supplementary material (sheet: info-reactions). Second, the reactions of Eqs. (1) and (2) only involve the phases that can be in equilibrium with each other, i.e., only the phases involving neighboring oxidation states are allowed in a reaction, making the predictions from both methods II and III similar. For example, the oxidations in the Cr–O system are from Cr to Cr_2O_3 and then to Cr_5O_{12} with increasing oxygen content, whereas the oxidation from Cr to Cr_5O_{12} is excluded; a complete list of the reactions is given in the Excel file of the supplementary material (sheet: info-reactions).

As an example, one of the Thermo-Calc macro files (i.e., the tcm files) to predict the Al_2O_3 Ellingham diagram using method II is shown in Table S1 of the supplementary material, which includes the phases of α-Al_2O_3 (both solid and liquid corundum), δ-Al_2O_3, γ-Al_2O_3, κ-Al_2O_3, Al (both solid and liquid), and all gas species (included but dormant) available in SSUB5, which are all relevant to the reaction of $\frac{4}{3}Al(s \text{ or } l) + O_2(g) = \frac{2}{3}Al_2O_3(s \text{ or } l)$. Following the equilibrium calculations, the P_{O_2} value (in Torr) is determined by Eq. (6); see also the function in the tcm file of the supplementary material.

III. RESULTS AND DISCUSSION

A. Ellingham diagrams of binary oxides

As an example, Fig. 1 shows the predicted Fe–O Ellingham diagram using both method II (Eq-reaction) and method III (Eq-system); cf., Sec. II B. Figure 1(a) (by method III) clearly identifies the predicted phase regions, including the gas phase region, while Fig. 1(b) (by method III) shows, in principle, the individual lines for the reactions of interest. Note that the associated phase regions in Fig. 1(b) are identical to those in Fig. 1(a). The red-dashed lines
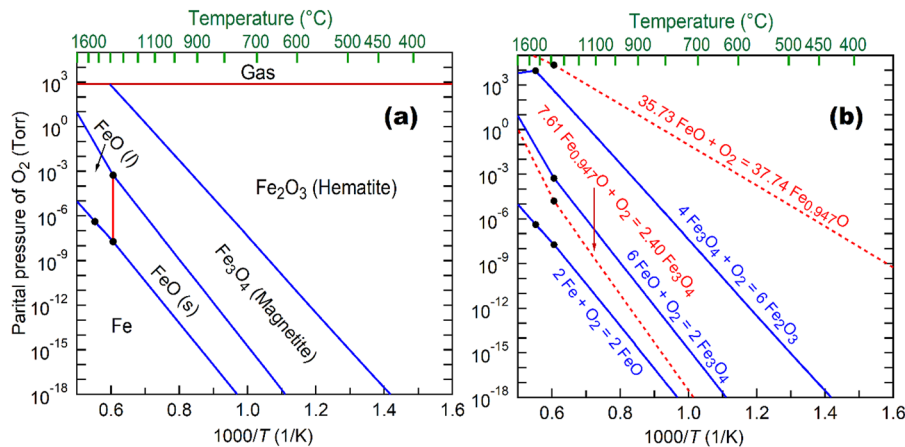

FIG. 1. Fe–O Ellingham diagram predicted by (a) method II (Eq-reaction) and (b) method III (Eq-system). The black dots indicate the solid/solid, solid/liquid, or liquid/gas phase transitions. The blue lines in both diagrams are identical, and the red-dashed lines indicate the reactions to form nonstable oxides (ignored in the present work).

in Fig. 1(b) are for reference only, since the nonstable $Fe_{0.947}O$ was ignored in the present work. The blue-solid lines in both Figs. 1(a) and 1(b) are identical, indicating that both methods II and III predict the same results. In addition, the black dots in both diagrams indicate the three-phase equilibria due to solid/solid, solid/liquid, or liquid/gas phase transitions. For example, there are two black dots for the reaction of $2Fe + O_2 = 2FeO$, representing the three-phase equilibria of "FeO (l), Fe (l), and Fe ($s3$)" and "FeO (l), FeO (s), and Fe ($s3$)" with the (T, P_{O_2}) values at (1811 K, 4.06×10^{-7} Torr) and (1650 K, 1.94×10^{-8} Torr), respectively. A complete list of the possible three-phase equilibria for all the reactions is given in the Excel file of the supplementary material (sheet: info-reactions).

Figure 2 summarizes the predicted Ellingham diagrams for the 137 reactions to form binary oxides. The data underlying these plots are given in the Excel file of the supplementary material (sheet: TP-data). 74 of them belong to reactions following *scenario one* [cf., Eq. (1)] and 63 to reactions following *scenario two* [cf., Eq. (2)]. The top of Fig. 2 at higher P_{O_2} contains the metals (elements) that

are the hardest to oxidize, while at the bottom of Fig. 2, at lower P_{O_2}, are the metals (elements) that are the easiest to oxidize. The P_{O_2} values at a given temperature can, hence, be used to rank the thermodynamic stability, i.e., the oxide-forming ability, of the oxides. The lower the P_{O_2} value, the higher the oxide-forming ability, and vice versa. Such a ranking shows that the most stable binary oxide is Tb_2O_3, associated with the reaction of $\frac{4}{3}Tb + O_2 = \frac{2}{3}Tb_2O_3$, which is the lowest line in the diagram, implying that the f-element Tb can reduce all other oxides. The most nonstable oxide is Au_2O_3, indicating that the reaction $\frac{4}{3}Au + O_2 = \frac{2}{3}Au_2O_3$ to form Au_2O_3 on the top of Fig. 2 is next to impossible as it occurs at extremely high P_{O_2} values ($>6 \times 10^{10}$ Torr). The commonly observed oxides Cr_2O_3 in stainless steel and Al_2O_3 in nickel-based superalloy are easily formed due to the lower P_{O_2} values required; see Fig. 2. It is worth mentioning that most lines in Fig. 2 are almost straight, except for two reactions exhibiting sharp kinks: $50WO_{2.96} + O_2 = 50WO_3$ (labeled as $WO_{2.96} \leftrightarrow WO_3$ in Fig. 2) and $18.02MoO_{2.889} + O_2 = 18.02MoO_3$ ($MoO_{2.889} \leftrightarrow MoO_3$). The kinks arise due to large Gibbs energy dif-
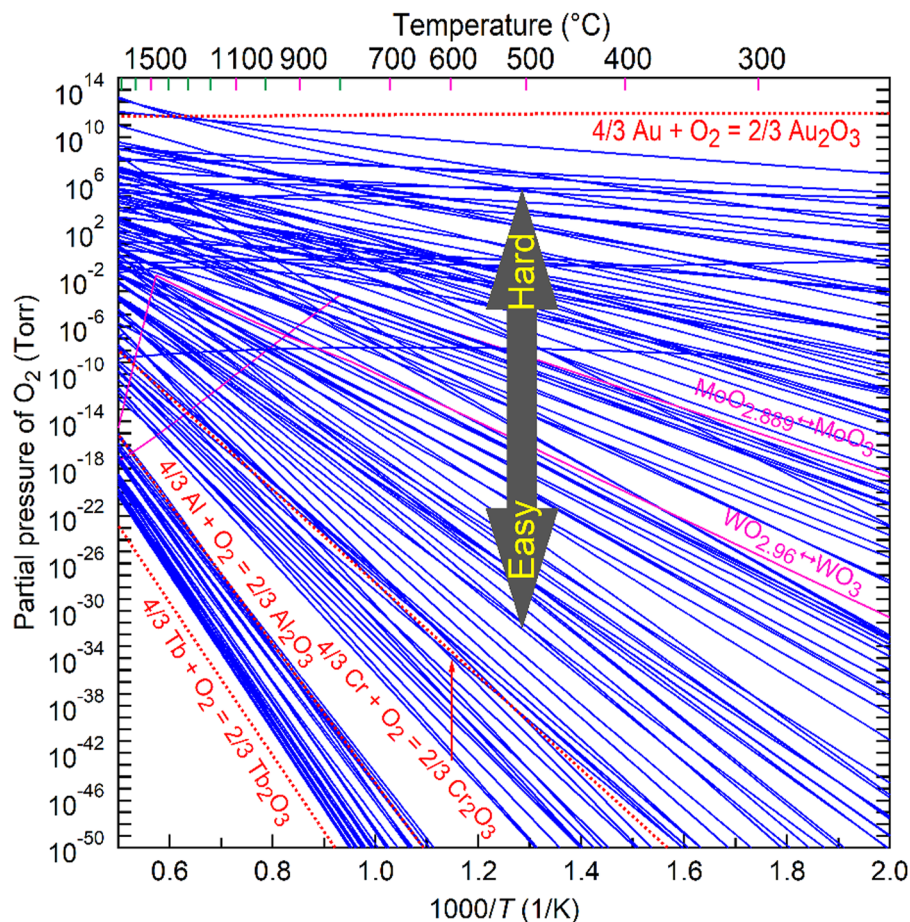
FIG. 2. Overview of the predicted Ellingham diagrams denoting the formation of 137 binary oxides. Note that the data plotted on this diagram are shown in the Excel file of the supplementary material (sheet: TP-data), with each reaction number listed in the Excel sheet: info-reactions, and one example of plots to form Ag_2O in the sheet: TP-data. Note also that the $\log_{10} P_{O_2}$ values at 1100 K for these reactions are plotted in Fig. 3. The dashed red lines label four key reactions, and the magenta lines label the two reactions exhibiting sharp kinks.
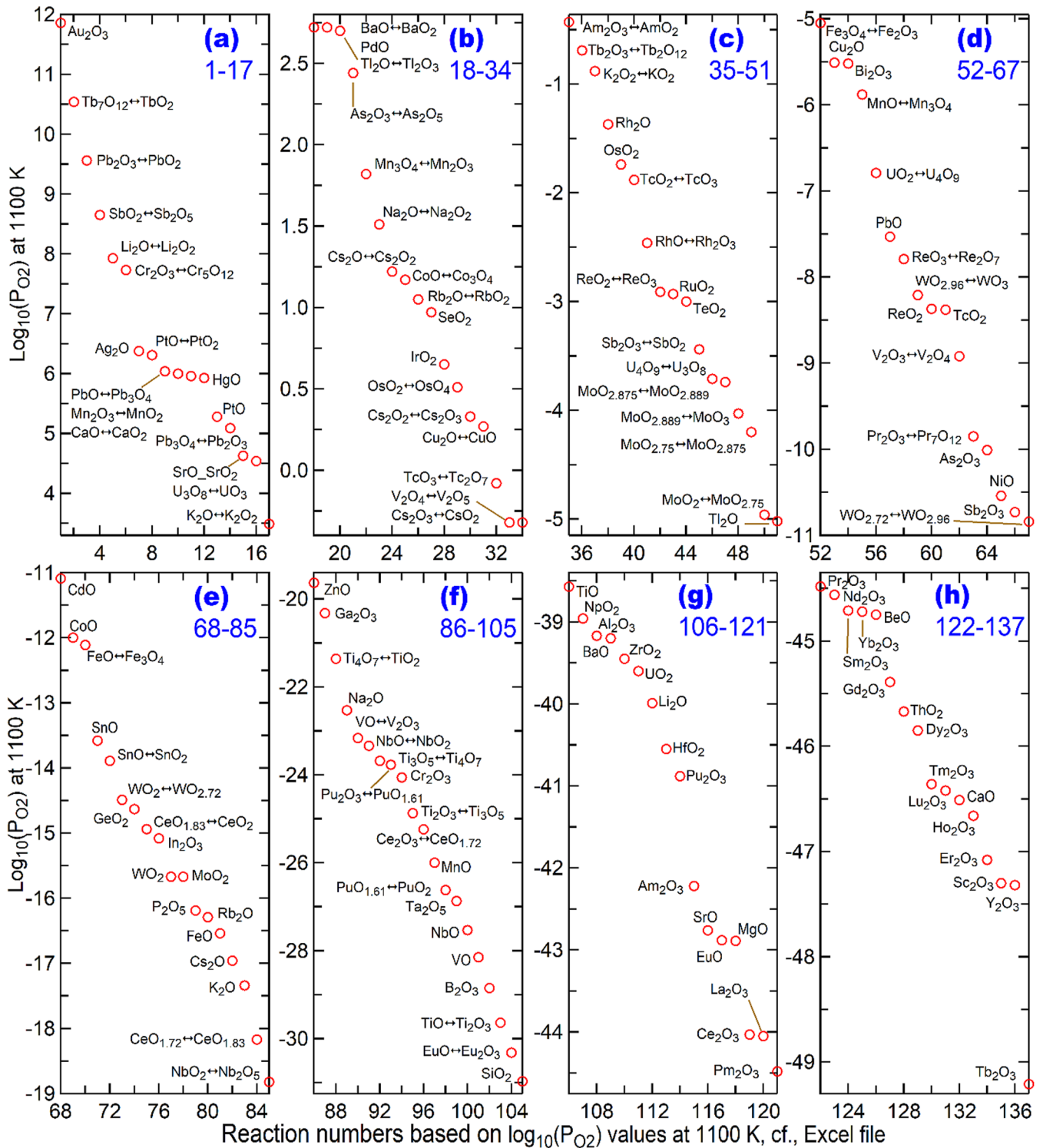
FIG. 3. $\log_{10} P_{O_2}$ values at 1100 K for the reactions in *scenario one* (74 reactions indicated by one oxide) and *scenario two* (63 reactions indicated by two oxides separated by "↔"). The $\log_{10} P_{O_2}$ values from high to low are shown in panels (a)–(h) with decreasing $\log_{10} P_{O_2}$ values. The horizontal axis corresponds to the reaction numbers listed in the Excel file of the supplementary material, which are ordered based on the $\log_{10} P_{O_2}$ values.

25 August 2024 12:21:43

ferences between the solids WO_3 and MoO_3 and their respective liquids.

To facilitate the analysis, Fig. 3 depicts the $\log_{10} P_{O_2}$ values with P_{O_2} in Torr at 1100 K for the 137 reactions. The exact values are given in the Excel file of the supplementary material (sheet: info-reactions). At 1100 K, the highest $\log_{10} P_{O_2}$ (=11.86) is for the formation of Au_2O_3 and the lowest $\log_{10} P_{O_2}$ (=−49.21) is for the formation of Tb_2O_3. In general, the $\log_{10} P_{O_2}$ (or P_{O_2}) values increase with increasing oxygen content for a given system at a given temperature. For example, the $\log_{10} P_{O_2}$ values in the Ti–O system increase from −38.57 to −21.36 at 1100 K with increasing oxygen content from the formation of TiO to Ti_2O_3, Ti_3O_5, Ti_4O_7, and up to TiO_2; see also the Excel file of the supplementary material. Nonetheless, at a given temperature, such as 1100 K, the $\log_{10} P_{O_2}$ values do not always increase with increasing oxygen content when metastable oxides exist. These cases include the metals K, Mn, Mo, Rh, Sn, Cs, Re, and Pu. For example, the $\log_{10} P_{O_2}$ values are −17.34, 3.49, and −0.88 at 1100 K for the reactions of $4K + O_2 = 2K_2O$, $2K_2O + O_2 = 2K_2O_2$, and $K_2O_2 + O_2 = 2KO_2$, respectively; see also the Excel file of the supplementary material (sheet: info-reactions) as well as the calculated K–O pressure–temperature phase diagram in Fig. S1 of the supplementary material.

To illustrate the trends, Table I shows the $\log_{10} P_{O_2}$ values at 1100 K in the Periodic Table for the 74 *scenario one* reactions, cf., Eq. (1) in colors. The "reactive" elements that form oxides easily are colored green and with lower $\log_{10} P_{O_2}$ values, including the f-block and group IIIB elements (lanthanides, actinides, Sc, and Y) and their neighbors in group IIA (alkaline earth metals) and group IVB (Ti, Zr, and Hf), and the elements Al and Li. These reactive elements readily form very stable oxides such as Tb_2O_3, Y_2O_3, Sc_2O_3, Er_2O_3, Ho_2O_3, and CaO; see Fig. 3. Table I indicates that the "noble" elements are colored red. They require higher $\log_{10} P_{O_2}$ values to be oxidized, including the coinage metals (Cu, Ag, and especially Au), Pt-group elements (Ru, Rh, Pd, Os, Ir, and Pt), and Hg and

Se. These noble elements could form oxides at high P_{O_2} values (e.g., $\log_{10} P_{O_2} > 0$ at 1100 K) and are readily reduced, for example, from the formed oxides of Au_2O_3, Ag_2O, HgO, PtO, PdO, SeO_2, and IrO_2, as shown in Figs. 3(a) and 3(b).

Note that Hensling *et al.*[1] have used the present data (from a preprint of our work[42]) to analyze oxygen pressures required to achieve specific oxidation states of all elements relevant to epitaxial film growth.

B. Understanding oxide-forming ability by correlation analysis

Although the order of oxidation shown in Fig. 3 qualitatively follows the order of half-cell reactions in redox chemistry[43] as well as other trends taught in chemistry, in the present work we apply a modern machine learning (ML) algorithm to identify how it correlates with 42 features/properties of the elements. Oxide-forming ability (represented by, for example, the $\log_{10} P_{O_2}$ values shown in Table I) was analyzed in terms of the sequential feature selection (SFS) method using a suitable machine learning (ML) algorithm.[44] Based on our previous work[44] and the present examinations, the selected ML algorithm is Gaussian Process Regression (GPR) with the kernel function of Matern52[45] as implemented in the software MATLAB (version R2021b). The presently examined features include the quantities of pure elements related to

- Periodic Table: e.g., atomic number, period, group, and Mendeleev number (M_Num2).
- Electronic configurations: the filled and unfilled s, p, d, f, and total valence electrons.
- Atomic size: e.g., covalent radius, van der Waals atomic radius, and atomic volume.
- Physical properties: e.g., thermal conductivity, electrical conductivity, electron density, electron affinity, and electronegativity (EleNeg).

TABLE I. Predicted $\log_{10} P_{O_2}$ values at 1100 K for the reactions in *scenario one* to form binary oxides, where the green–yellow–red color scale is used to mark the $\log_{10} P_{O_2}$ values from low to high. Green elements are easy to oxidize and red are not.

Li	Be											B	C	N	O
-40.0	-44.7											-28.9			
Na	Mg											Al	Si	P	S
-22.5	-42.9											-39.2	-31.0	-16.2	
K	Ca	Sc	Ti	V	Cr	Mn	Fe	Co	Ni	Cu	Zn	Ga	Ge	As	Se
-17.3	-46.5	-47.3	-38.6	-28.2	-24.1	-26.0	-16.5	-12.0	-10.5	-5.5	-19.6	-20.3	-14.6	-10.0	1.0
Rb	Sr	Y	Zr	Nb	Mo	Tc	Ru	Rh	Pd	Ag	Cd	In	Sn	Sb	Te
-16.3	-42.8	-47.3	-39.4	-27.5	-15.7	-8.4	-2.9	-1.4	2.7	6.4	-11.1	-15.1	-13.6	-10.7	-3.0
Cs	Ba		Hf	Ta	W	Re	Os	Ir	Pt	Au	Hg	Tl	Pb	Bi	Po
-17.0	-39.2		-40.6	-26.9	-15.7	-8.4	-1.7	0.6	5.3	11.9	5.9	-5.0	-7.5	-5.5	

La	Ce	Pr	Nd	Pm	Sm	Eu	Gd	Tb	Dy	Ho	Er	Tm	Yb	Lu
-44.0	-44.0	-44.5	-44.6	-44.5	-44.7	-42.9	-45.4	-49.2	-45.8	-46.7	-47.1	-46.4	-44.7	-46.4
Ac	Th	Pa	U	Np	Pu	Am								
	-45.7		-39.6	-39.0	-40.9	-42.2								

- Thermochemical properties: e.g., the heat of sublimation, the heat of vaporization (VaporHeat); heat capacity, standard entropy at 298 K (S298), melting temperature (MeltingT), and boiling temperature.
- Elastic properties: bulk modulus, shear modulus, and Young's modulus.

All 42 of these features of the elements are explained in Table S1 of the supplementary material, with their values given in the Excel file of the supplementary material (sheet: 42_features).

After around four iterations using MATLAB between the SFS processes and the GPR verifications by means of the five-fold cross-validation (CV) for 500 times (see details in Ref. 44), the ranked features based on their statistical significances are listed in Table S1 and Fig. S2 of the supplementary material, showing the overall mean absolute error (MAE) values of $\log_{10} P_{O_2}$ (for reactions in *scenario one*) with respect to the combined features starting from the single feature of NdVal (the number of *d* valence electrons). Here, the feature NdVal has the highest correlation with respect to $\log_{10} P_{O_2}$ based on the R^2 values of linear fit-of-goodness; see Table S2 of the supplementary material. Figure 4 shows that there exists a strong correlation between the *d* valence electrons (NdVal) and $\log_{10} P_{O_2}$, with $R^2 = 0.73$ and MAE = 7.2. Adding more features in addition to NdVal results in an increase in R^2 and a decrease in MAE. Table II lists the optimal set of 15 features, reaching an overall MAE = 2.00 (Fig. S2) and $R^2 = 0.98$ (not shown). In particular, the top six features that decrease the MAE fastest (cf., Fig. S2 and Table II) are NdVal, NsVal, M_Num2, Group, MeltingT, and S298. The ML analysis shows that the trends observed in the Periodic Table (Table I) are, in fact, correlated with the electronic structures of pure elements, such as the features of NdVal, NsVal, M_Num2, and Group. In addition, MeltingT and S298 are also key features to tailor oxide-forming ability, plus minor effects of the other thermochemical and physical properties such as the heat of vaporization, heat capacity, and electronegativity; see Fig. S2 and Table II.

As one of the examinations concerning the optimal set of 15 features, Fig. 5 shows the predicted $\log_{10} P_{O_2}$ values (for reactions in *scenario one* at 1100 K) by GPR using the five-fold CV, illustrating a good agreement with the original $\log_{10} P_{O_2}$ values with the fitted $R^2 = 0.976 \pm 0.006$. The outliers are the formation of Cr_2O_3, HgO, BeO, and Ag_2O based on at least 2000 machine learning trainings; see detailed methodology in Ref. 44. Note that these outliers may
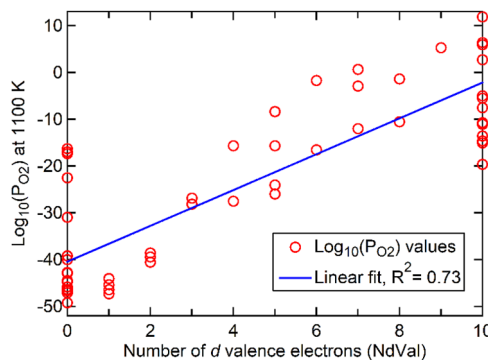

FIG. 4. Predicted $\log_{10} P_{O_2}$ values for the reactions in *scenario one* [cf., Eq. (1)] with respect to the numbers of *d* valence electrons (NdVal) of pure elements.

be caused by Gibbs energy errors in the SSUB5 database. Figure 5 indicates the statistical significance of the present 15 features (Table II), which correlate with the oxide-forming ability of pure elements.

The present correlation analysis demonstrates that (i) electronic structures of pure elements are the key in affecting their oxide-forming ability, resulting in the clear trends regarding the $\log_{10} P_{O_2}$ values in the Periodic Table in Table I; and (ii) thermochemical properties such as MeltingT and S298 are weakly correlated with oxide-forming ability.

C. Examining oxide-forming ability in multicomponent alloys

Ellingham diagrams of binary oxides are fundamental to understand and predict oxide-forming ability in multicomponent alloys. Taking concentrated alloys as examples, Fig. 6 shows the predicted phases as a function of P_{O_2} for the equimolar high entropy alloy AlCoCrFeNi at 1000 K and the Fe–20Cr–20Ni (wt. %) alloy at 873 K, where the CALPHAD results were performed by the Thermo-Calc software and the TCFE8 database.[39] Figure 6(a) shows that with increasing P_{O_2} from 10^{-40} Torr (i.e., $\log_{10} P_{O_2} = -40$), first the Al_2O_3-rich corundum forms and then the Cr_2O_3-rich corundum appears ($P_{O_2} > 10^{-27}$ Torr or $\log_{10} P_{O_2} > -27$) in AlCoCrFeNi, while the other

TABLE II. The 15 elemental features that most strongly correlate with the ease of oxidation (i.e., the $\log_{10} P_{O_2}$ value) based on the sequential feature selection method using the Gaussian process regression algorithm, where the top six features are highlighted by bold and italic texts and the explanations of these features are given in Table S2 of the supplementary material.

| Category	Selected elemental features
Electronic configurations	***NdVal (number of d valence electrons), NsVal,*** NfUnfill (number of unfilled f valence electrons), NdUnfill
Positions in the Periodic Table	***M_Num2 (Mendeleev number), Group,*** Period
Thermochemical properties	***MeltingT (melting temperature), S298 (standard entropy at 298 K),*** VaporHeat (vaporization heat), CohEnergy, Heat_Capacity, BoilingT
Physical properties	EleNeg_Miedema, Ion_Pot_3
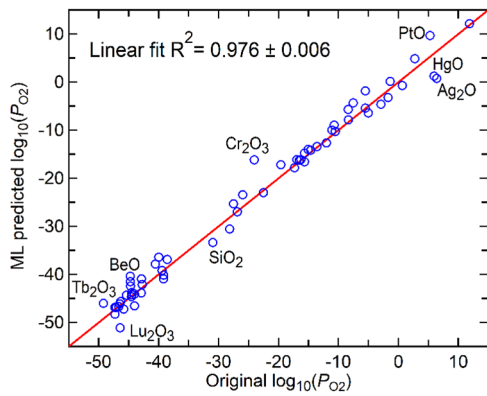
FIG. 5. Machine learning (ML) fitting of the $\log_{10} P_{O_2}$ values using the Gaussian process regression with the kernel function of Matern52, 15 features, and the five-fold CV. This figure shows only one of the fittings. The outliers are Cr_2O_3, HgO, BeO, and Ag_2O, and the overall R^2 value is based on 2000 ML trainings.

oxides such as FeO and NiO are not observed. The CALPHAD-based calculations agree with experimental observations where the formed oxides in AlCoCrFeNi are mainly Al_2O_3 and Cr_2O_3.[32,46] Table I shows that $\log_{10} P_{O_2} = -39.2$ and -24.1, respectively, for the formations of Al_2O_3 and Cr_2O_3 at 1100 K, agreeing well with experimental observations. The unobserved oxides are due mainly to the higher P_{O_2} values required to form, e.g., $\log_{10} P_{O_2} = -10.5$ for NiO,
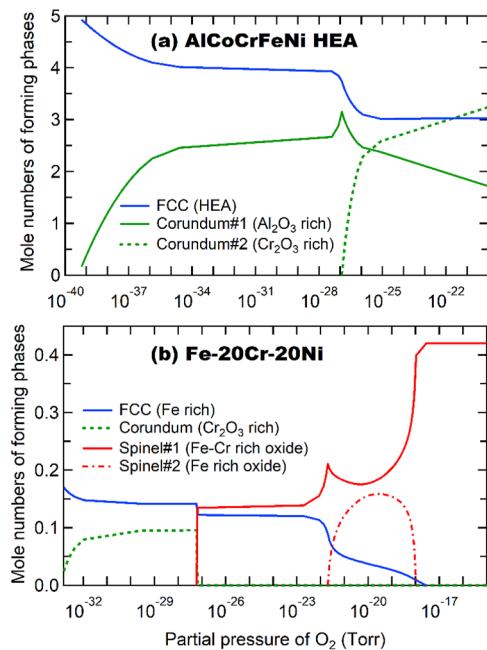

FIG. 6. Predicted phases of two alloys as a function of the partial pressure of O_2 (P_{O_2}) based on the TCFE8 database: (a) Equimolar AlCoCrFeNi at 1000 K and (b) Fe–20Cr–20Ni (wt. %) at 873 K. Experimentally, the formed oxides in AlCoCrFeNi after 25 h oxidation at 1000 K are mainly Al_2O_3 and Cr_2O_3,[32,46] and the formed oxide in Fe–20Cr–20Ni after 1000 h oxidation in the air and at 873 K is mainly Cr_2O_3.[47]

$\log_{10} P_{O_2} = -12.0$ for CoO, and $\log_{10} P_{O_2} = -16.5$ for FeO at 1100 K; cf., Table I as well as the Excel file of the supplementary material.

The analysis of Fe–20Cr–20Ni is similar. Figure 6(b) shows that with increasing P_{O_2} from $\log_{10} P_{O_2} = -31$, first the Cr_2O_3-rich corundum appears in Fe–20Cr–20Ni at 873 K, then the Fe–Cr rich and the Fe-rich spinel appear when $\log_{10} P_{O_2} > 10^{-28}$ and 10^{-22}, respectively. Experimentally, the observed oxides are mainly Cr_2O_3 at 873 K after 1000 h oxidation in the air.[47] The unobserved NiO in both CALPHAD predictions and experiments is due mainly to the high P_{O_2} value to form NiO, while the unobserved FeO is due mainly to the relatively high P_{O_2} value required; for example, $\log_{10} P_{O_2} = -24.1$ for Cr_2O_3, $\log_{10} P_{O_2} = -16.5$ for FeO, $\log_{10} P_{O_2} = -10.5$ for NiO at 1100 K as shown in Table I as well as the Excel file of the supplementary material.

IV. SUMMARY AND CONCLUDING REMARKS

This work provides a calculation of Ellingham diagrams for 137 binary oxides based on a comprehensive thermodynamic study, which can be used to understand and control the oxidation state of constituents for material synthesis and material degradation. It shows that the "reactive" elements that form oxides easily are the f-block elements (lanthanides and actinides), the elements in groups II, III, and IV (alkaline earth, Sc, Y, and Ti, Zr, and Hf), and the elements Al and Li. In contrast, the "noble" elements that are difficult to oxidize are coinage metals (Cu, Ag, and especially Au), Pt-group elements, and Hg and Se. Application of correlation analysis to the calculated Ellingham diagrams reveals that the most strongly correlated attributes of the 42 considered are the d- and s-valence electrons, the Mendeleev number, and the groups of pure elements. These features make the Periodic Table a great tool to qualitatively assess the ease of oxidation of pure elements. In addition, thermochemical properties such as melting points and standard entropy at 298 K are also weakly correlated with the ease of oxidation. As an application of Ellingham diagrams, the thermodynamic stabilities of the Fe–20Cr–20Ni alloy (in wt. %) and the equimolar AlCoCr-FeNi in oxidizing environments are predicted using the CALPHAD approach. The predicted oxides are in accordance with experimental observations, which can be understood by the calculated Ellingham diagrams.

Although Ellingham diagrams can qualitatively suggest whether a given oxide system will oxidize or reduce at elevated temperatures, some cautionary comments are in order. To facilitate comparison, an Ellingham diagram is built under the conditions of a total pressure of one atmosphere by consuming one mole of oxygen (O_2). These conditions may differ from the growth conditions of oxides by thin film techniques such as MBE,[37] where materials are usually synthesized at a fixed partial pressure of oxygen rather than a fixed total pressure. The MBE process behaves like either an open or a closed system depending on the fluxes of metallic elements, as has been discussed in the thermodynamics of MBE (TOMBE) diagrams.[25,37] In addition, the Ellingham diagram is based on thermodynamics, but for film growth, kinetic factors could also be important. An Ellingham diagram does not quantify the rate of reaction as well as the effect of elemental diffusivity in both alloys and oxides, which need to be considered for a complete analysis.[31,35] Solid solubilities may exist in oxides, and complex ternary and higher-order oxides may be formed. Such effects were excluded

in the Ellingham diagrams calculated here. In addition, internal oxidation in the subsurface may also need to be considered to study the oxidation and hot corrosion protection of alloys.[35,48]

SUPPLEMENTARY MATERIAL

See the supplementary material for raw data in the Excel file, the Thermo-Calc macro file (i.e., the tcm file) to predict the Al_2O_3 Ellingham diagram, elemental features (descriptors) and their ranks, calculated K–O pressure–temperature phase diagram, and examination of the combined features.

ACKNOWLEDGMENTS

AUTHOR DECLARATIONS

Conflict of Interest

The authors have no conflicts to disclose.

Author Contributions

Shun-Li Shang: Data curation (lead); Formal analysis (lead); Investigation (lead); Methodology (lead); Writing – original draft (lead); Writing – review & editing (equal). **Shuang Lin**: Data curation (supporting); Investigation (supporting); Writing – review & editing (equal). **Michael C. Gao**: Methodology (supporting); Supervision (supporting); Writing – review & editing (supporting). **Darrell G. Schlom**: Conceptualization (lead); Formal analysis (supporting); Methodology (supporting); Writing – review & editing (lead). **Zi-Kui Liu**: Conceptualization (supporting); Formal analysis (supporting); Funding acquisition (lead); Writing – review & editing (supporting).

DATA AVAILABILITY

Most of the raw data used in the present study are available in the supplementary material Excel file, and the other data are available from the corresponding author upon reasonable request.

REFERENCES

[1]F. V. E. Hensling, W. Braun, D. Y. Kim, L. N. Majer, S. Smink, B. D. Faeth, and J. Mannhart, "State of the art, trends, and opportunities for oxide epitaxy," APL Mater. **12**(4), 40902 (2024).

[2]F. H. Stott, G. C. Wood, and J. Stringer, "The influence of alloying elements on the development and maintenance of protective scales," Oxid. Met. **44**(1–2), 113–145 (1995).

[3]B. Gorr, S. Schellert, F. Müller, H.-J. Christ, A. Kauffmann, and M. Heilmaier, "Current status of research on the oxidation behavior of refractory high entropy alloys," Adv. Eng. Mater. **23**(5), 2001047 (2021).

[4]J. Sun, M. R. Barone, C. S. Chang, M. E. Holtz, H. Paik, J. Schubert, D. A. Muller, and D. G. Schlom, "Growth of $PdCoO_2$ by ozone-assisted molecular-beam epitaxy," APL Mater. **7**(12), 121112 (2019).

[5]C.-L. Jia, K. W. Urban, M. Alexe, D. Hesse, and I. Vrejoiu, "Direct observation of continuous electric dipole rotation in flux-closure domains in ferroelectric $Pb(Zr,Ti)O_3$," Science **331**(6023), 1420–1423 (2011).

[6]G. H. Jonker and J. H. Van Santen, "Ferromagnetic compounds of manganese with perovskite structure," Physica **16**(3), 337–349 (1950).

[7]A. J. Hauser, R. E. A. Williams, R. A. Ricciardo, A. Genc, M. Dixit, J. M. Lucy, P. M. Woodward, H. L. Fraser, and F. Yang, "Unlocking the potential of half-metallic Sr_2FeMoO_6 films through controlled stoichiometry and double-perovskite ordering," Phys. Rev. B **83**(1), 014407 (2011).

[8]J. Wang, J. B. Neaton, H. Zheng, V. Nagarajan, S. B. Ogale, B. Liu, D. Viehland, V. Vaithyanathan, D. G. Schlom, U. V. Waghmare, N. A. Spaldin, K. M. Rabe, M. Wuttig, and R. Ramesh, "Epitaxial $BiFeO_3$ multiferroic thin film heterostructures," Science **299**(5613), 1719–1722 (2003).

[9]J. H. Lee, X. Ke, R. Misra, J. F. Ihlefeld, X. S. Xu, Z. G. Mei, T. Heeg, M. Roeckerath, J. Schubert, Z. K. Liu, J. L. Musfeldt, P. Schiffer, and D. G. Schlom, "Adsorption-controlled growth of $BiMnO_3$ films by molecular-beam epitaxy," Appl. Phys. Lett. **96**(26), 262905 (2010).

[10]A. Schilling, M. Cantoni, J. D. Guo, and H. R. Ott, "Superconductivity above 130 K in the Hg–Ba–Ca–Cu–O system," Nature **363**(6424), 56–58 (1993).

[11]Y. Ma, A. Edgeton, H. Paik, B. D. Faeth, C. T. Parzyck, B. Pamuk, S. Shang, Z.-K. Liu, K. M. Shen, D. G. Schlom, and C. Eom, "Realization of epitaxial thin films of the topological crystalline insulator Sr_3SnO," Adv. Mater. **32**(34), 2000809 (2020).

[12]J. Suntivich, H. A. Gasteiger, N. Yabuuchi, H. Nakanishi, J. B. Goodenough, and Y. Shao-Horn, "Design principles for oxygen-reduction activity on perovskite oxide catalysts for fuel cells and metal–air batteries," Nat. Chem. **3**(7), 546–550 (2011).

[13]J. Suntivich, K. J. May, H. A. Gasteiger, J. B. Goodenough, and Y. Shao-Horn, "A perovskite oxide optimized for oxygen evolution catalysis from molecular orbital principles," Science **334**(6061), 1383–1385 (2011).

[14]G. Wan, J. W. Freeland, J. Kloppenburg, G. Petretto, J. N. Nelson, D.-Y. Kuo, C.-J. Sun, J. Wen, J. T. Diulus, G. S. Herman, Y. Dong, R. Kou, J. Sun, S. Chen, K. M. Shen, D. G. Schlom, G.-M. Rignanese, G. Hautier, D. D. Fong, Z. Feng, H. Zhou, and J. Suntivich, "Amorphization mechanism of $SrIrO_3$ electrocatalyst: How oxygen redox initiates ionic diffusion and structural reorganization," Sci. Adv. **7**(2), eabc7323 (2021).

[15]I. Nagai, N. Shirakawa, S. Ikeda, R. Iwasaki, H. Nishimura, and M. Kosaka, "Highest conductivity oxide $SrMoO_3$ grown by a floating-zone method under ultralow oxygen partial pressure," Appl. Phys. Lett. **87**(2), 024105 (2005).

[16]T. Kuznetsova, J. Roth, J. Lapano, A. Pogrebnyakov, and R. Engel-Herbert, "Growth of $SrMoO_3$ thin films by suboxide molecular beam epitaxy," J. Vac. Sci. Technol. A **41**(5), 53412 (2023).

[17]L. Guo, S.-L. Shang, N. Campbell, P. G. Evans, M. Rzchowski, Z.-K. Liu, and C.-B. Eom, "Searching for a route to synthesize in situ epitaxial $Pr_2Ir_2O_7$ thin films with thermodynamic methods," npj Comput. Mater. **7**(1), 144 (2021).

[18]H. J. T. Ellingham and J. Soc, "Transactions and communications," Chem. Ind. **63**(5), 125–160 (1944).

[19]D. G. Schlom and J. S. Harris, in *Mol. Beam Ep.–Appl. To Key Mater.*, edited by R. F. C. Farrow (William Andrew Publishing/Noyes, Park Ridge, 1995), pp. 505–622.

[20]D. G. Schlom, A. F. Marshall, J. T. Sizemore, Z. J. Chen, J. N. Eckstein, I. Bozovic, K. E. Von Dessonneck, J. S. Harris, and J. C. Bravman, "Molecular beam epitaxial growth of layered Bi–Sr–Ca–Cu–O compounds," J. Cryst. Growth **102**(3), 361–375 (1990).

[21]H. Paik, Z. Chen, E. Lochocki, A. Seidner H, A. Verma, N. Tanen, J. Park, M. Uchida, S. Shang, B.-C. C. Zhou, M. Brützam, R. Uecker, Z.-K. K. Liu, D. Jena, K. M. Shen, D. A. Muller, D. G. Schlom, A. Seidner H, A. Verma, N. Tanen, J. Park, M. Uchida, S. Shang, B.-C. C. Zhou, M. Brützam, R. Uecker, Z.-K. K. Liu, D. Jena,

K. M. Shen, D. A. Muller, and D. G. Schlom, "Adsorption-controlled growth of La-doped BaSnO$_3$ by molecular-beam epitaxy," APL Mater. **5**(11), 116107 (2017).

[22]J. F. Ihlefeld, W. Tian, Z. K. Liu, W. A. Doolittle, M. Bernhagen, P. Reiche, R. Uecker, R. Ramesh, and D. G. Schlom, IEEE Trans. Ultrason. Ferroelectr. Freq. Control **56**, 1528–1533 (2009).

[23]C. M. Brooks, R. Misra, J. A. Mundy, L. A. Zhang, B. S. Holinsworth, K. R. O'Neal, T. Heeg, W. Zander, J. Schubert, J. L. Musfeldt, Z. K. Liu, D. A. Muller, P. Schiffer, and D. G. Schlom, "The adsorption-controlled growth of LuFe$_2$O$_4$ by molecular-beam epitaxy," Appl. Phys. Lett. **101**(13), 132907 (2012).

[24]E. H. Smith, J. F. Ihlefeld, C. A. Heikes, H. Paik, Y. Nie, C. Adamo, T. Heeg, Z. K. Liu, and D. G. Schlom, "Exploiting kinetics and thermodynamics to grow phase-pure complex oxides by molecular-beam epitaxy under continuous codeposition," Phys. Rev. Mater. **1**(2), 023403 (2017).

[25]H. P. Nair, Y. Liu, J. P. Ruf, N. J. Schreiber, S.-L. Shang, D. J. Baek, B. H. Goodge, L. F. Kourkoutis, Z.-K. Liu, K. M. Shen, and D. G. Schlom, "Synthesis science of SrRuO$_3$ and CaRuO$_3$ epitaxial films with high residual resistivity ratios," APL Mater. **6**(4), 046101 (2018).

[26]M. Sainz, A. Mazzoni, E. Aglietti, and A. Caballero, "Thermochemical stability of spinel (MgO · Al$_2$O$_3$) under strong reducing conditions," Mater. Chem. Phys. **86**(2–3), 399–408 (2004).

[27]E. Niwa, K. Wakai, T. Hori, K. Yashiro, J. Mizusaki, and T. Hashimoto, "Thermodynamic analyses of structural phase transition of Pr$_2$NiO$_{4+\delta}$ involving variation of oxygen content," Thermochim. Acta **575**, 129–134 (2014).

[28]K. Ishizaki, "Phase diagrams under high total gas pressures—Ellingham diagrams for hot isostatic press processes," Acta Metall. Mater. **38**(11), 2059–2066 (1990).

[29]W. Smeltzer and D. Young, "Oxidation properties of transition metals," Prog. Solid State Chem. **10**(PART 1), 17–54 (1975).

[30]W. M. Mellor, K. Kaufmann, O. F. Dippo, S. D. Figueroa, G. D. Schrader, and K. S. Vecchio, "Development of ultrahigh-entropy ceramics with tailored oxidation behavior," J. Eur. Ceram. Soc. **41**(12), 5791–5800 (2021).

[31]L. Backman and E. J. Opila, "Thermodynamic assessment of the group IV, V and VI oxides for the design of oxidation resistant multi-principal component materials," J. Eur. Ceram. Soc. **39**(5), 1796–1802 (2019).

[32]I. Roy, P. K. Ray, and G. Balasubramanian, "Modeling oxidation of AlCoCr-FeNi high-entropy alloy using stochastic cellular automata," Entropy **24**(9), 1263 (2022).

[33]C. W. Bale, E. Bélisle, P. Chartrand, S. A. Decterov, G. Eriksson, K. Hack, I.-H. Jung, Y.-B. Kang, J. Melançon, A. D. Pelton, C. Robelin, and S. Petersen, "FactSage thermochemical software and databases—Recent developments," Calphad **33**(2), 295–311 (2009).

[34]N. Birks, G. H. Meier, and F. S. Pettit, *Introduction to the High Temperature Oxidation of Metals*, 2nd ed. (Cambridge University Press, 2006).

[35]B. Gleeson, *Shreir's Corros.* (Elsevier, 2010), pp. 180–194.

[36]Z.-K. Liu, "First-principles calculations and CALPHAD modeling of thermodynamics," J. Phase Equilib. Diffus. **30**(5), 517–534 (2009).

[37]K. M. Adkison, S.-L. Shang, B. J. Bocklund, D. Klimm, D. G. Schlom, and Z.-K. Liu, "Suitability of binary oxides for molecular-beam epitaxy source materials: A comprehensive thermodynamic analysis," APL Mater. **8**(8), 081110 (2020).

[38]J. D. A. Simoni and A. P. Chagas, "Diagramas de Ellingham e de Van't Hoff: Algumas considerações," Quim. Nova **30**(2), 501–504 (2007).

[39]J.-O. Andersson, T. Helander, L. Höglund, P. Shi, and B. Sundman, "Thermo-Calc and DICTRA: Computational tools for materials science," Calphad **26**(2), 273–312 (2002).

[40]Scientific Group Thermodata Europe (SGTE), in *Landolt-Boernstein New Ser. Gr. IV*, edited by Lehrstuhl fuer Theoretische Huettenkunde (Springer Verlag, Berlin, Heidelberg, 1999).

[41]F. Tesfaye, D. Sukhomlinov, D. Lindberg, P. Taskinen, and G. Akdogan, "Thermal stabilities and properties of equilibrium phases in the Pt-Te-O system," J. Chem. Thermodyn. **106**, 47–58 (2017).

[42]S.-L. Shang, S. Lin, M. C. Gao, D. G. Schlom, and Z.-K. Liu, "Predictions and correlation analyses of Ellingham diagrams in binary oxides," arXiv: 2308.05837 (2023).

[43]C. E. Housecroft and A. G. Sharpe, *Inorganic Chemistry* (Prentice Hall, 2008).

[44]X. Chong, S.-L. Shang, A. M. Krajewski, J. D. Shimanek, W. Du, Y. Wang, J. Feng, D. Shin, A. M. Beese, and Z.-K. Liu, "Correlation analysis of materials properties by machine learning: Illustrated with stacking fault energy from first-principles calculations in dilute fcc-based alloys," J. Phys.: Condens. Matter **33**(29), 295702 (2021).

[45]C. E. Rasmussen and C. K. I. Williams, *Gaussian Processes for Machine Learning* (MIT Press, 2006).

[46]T. M. Butler and M. L. Weaver, "Oxidation behavior of arc melted AlCoCr-FeNi multi-component high-entropy alloys," J. Alloys Compd. **674**, 229–244 (2016).

[47]B. B. Newcomb, W. M. Stobbs, and E. Metcalfe, "A microstructural study of the oxidation of Fe–Ni–Cr alloys I. protective oxide growth," Philos. Trans. R. Soc. A **319**(1546), 191–218 (1986).

[48]A. Ross, S. Shang, H. Fang, G. Lindwall, X. L. Liu, W. Zhao, B. Gleeson, M. C. Gao, and Z. Liu, "Tailoring critical Al concentration to form external Al$_2$O$_3$ scale on Ni–Al alloys by computational approach," J. Am. Ceram. Soc. **105**(12), 7770–7777 (2022).

Supplementary Material for:

Ellingham diagrams of binary oxides

Shun-Li Shang,[1,2,*] Shuang Lin,[1] Michael C. Gao,[2] Darrell G. Schlom,[3,4,5] and Zi-Kui Liu[1]

[1] Department of Materials Science and Engineering, The Pennsylvania State University, University Park, Pennsylvania 16802, USA

[2] Materials Engineering and Manufacturing Directorate, National Energy Technology Laboratory, Albany, Oregon 97321, USA

[3] Department of Materials Science and Engineering, Cornell University, Ithaca, New York 14853, USA

[4] Kavli Institute at Cornell for Nanoscale Science, Ithaca, New York 14853, USA

[5] Leibniz-Institut für Kristallzüchtung, Max-Born-Str. 2, 12489 Berlin, Germany

* sus26@psu.edu (S. L. Shang)

The **Supplemental** Excel file includes the following three sheets:

- (1) Sheet "info-reactions":

  o Columns A and B list atomic numbers and names of pure elements.

  o Columns C and D list the possible oxides in the SSUB5 database as well as their names when available.

  o Column E (O-vs-M) lists the ratio of oxygen vs. metal (element) for each oxide.

  o Column F (log10_PO2_1100) lists the log (base 10) values of P_{O_2} at 1100 K. Note that for each M-O system, if the oxygen content (column E: "O-vs-M") increases, but the value of "Log10_PO2_1100" does not increase, this indicates that some oxides in this system are metastable. An example of such a P-T phase diagram can be seen in the K-O system.

  o Column G (Stable-or-not): After examining all phase diagrams for all the M-O systems by thermodynamic calculations, this column shows all the stable and metastable oxides (marked by "Yes") and the nonstable oxides (marked by "No").

  o Column I (Reaction) lists the reactions which are in *scenario one* (showing only one oxide) or in *scenario two* (showing two oxides separated by "_").

  o Column J (No_Reaction) lists the number of each reaction, corresponding the $\log_{10} P_{O_2}$ values at 1100 K from large to small in Column F ("log10_PO2_1100"), i.e., the list of reactions in Fig. 3. Note that these reaction numbers are also used to find the T-P data for the reactions in sheet "TP-data". For example, the T-P data of reaction no. 7 (i.e., "x7#AG2O1 vs. y7#AG2O1") are in Columns M and N in sheet "TP-data"; the T-P data for the last reaction no. 137 (i.e., "x137#O3TB2 vs. y137#O3TB2") are in the last two Columns JM and JN in sheet "TP-data".

- o Column K (Three-Phases-and-T-P) lists all the three-phase equilibrium points and the corresponding temperature (in K) and P_{O_2} values.

- **(2) Sheet "TP-data":**

  - o Note that (I) the column names starting with "x" indicate the inverse temperatures ($1000/T$, where T is in K) and the column names starting with "y" indicate the P_{O_2} values (in Torr), where the numbers after x or y are the reaction numbers as listed in Column J (No_Reaction) in sheet: info-reactions. The reactions in *scenario one* are marked by only one oxide after the symbol "#" and the reactions in *scenario two* are marked by two oxides separated by "_" after the symbol "#".

  - o Note that (II) the names of these oxides in this sheet are the same as those in the SSUB5 database. For example, columns A and B, which list the inverse temperatures ($1000/T$, where T is in K, marked by x1#AU2O3) and the P_{O_2} values (in Torr, marked by y1#AU2O3) for the reaction in *scenario one* to form Au_2O_3. As an example, the $\log_{10} P_{O_2}$ vs. $1000/T$ phase diagram is plotted for the formation of Ag_2O in this sheet.

- **(3) Sheet "42-features":**

  - o A list of the 42 elemental features examined in the present work together with the corresponding P_{O_2} values at 1100 K (column AR: logpo2), see the explanations of these features in Table S 2.

Table S1. An example of the Thermo-Calc macro file (i.e., the tcm file) to predict the Al_2O_3 Ellingham diagram using Method II.

```
go data
sw ssub5
def-ele AL O
get
go p-3
ch ph *=dor
ch ph AL_S AL_L  = e 1
ch ph CORUNDUM CORUNDUM_L AL2O3_DELTA AL2O3_GAMMA AL2O3_KAPPA  = e 1
s-c n(O)=2
s-c n(AL)=1.333333333
s-c p=1e5 t=2000
c-e
c-e
s-a-v 1 t 300 3000,,,,
step,,,,
post
e-sy f torr=acr(o2,gas)*p/133.33;
s-d-a x t-k
s-d-a y torr
s-a-ty y log
s-a-ty x inv
s-a-te x n 1/T
s-a-te y n PO2 (Torr)
s-la b
pl,,,,,,,
set_inter
```

Table S2. Elemental features/descriptors examined together with their goodness-of-fit R^2 values between the features and the $\log_{10}P_{O2}$ values at 1100 K for 74 reactions in *scenario one*. The numbers in the "Rank" column rank the statistical significances of the features to regulate $\log_{10}P_{O2}$ after iterations between the sequential feature selection and the predictions using the Gaussian process regression (with the kernel function of matern52)[1]. Note that the values of these features are given in the Supplemental Excel file (sheet: 42-features).

Rank	Features	R^2	Explanations
1	NdVal	0.727	Number of *d* valence electrons.
2	M_Num2	0.408	Mendeleev number (MN2, start from left bottom, down-top sequence)[2].
3	Group	0.065	Group of pure elements in the periodic table.
4	MeltingT	0.004	Melting temperature (in K) based on the collections by Kittel[3].
5	S298	0.073	Standard entropy at 298 K (in J/mol.K)[4]
6	NsVal	0.204	Number of *s* valence electrons.
7	NfUnfill	0.201	Number of unfilled *f* valence electrons.
8	Period	0.002	Group of pure elements in the periodic table.
9	VaporHeat	0.018	Vaporization heat (in kJ/mol) based on the collections of Wolfram Mathematica (WM); see "VaporizationHeat" in WM[5].
10	CohEnergy	0.030	Cohesive energy (in eV/atom) collected by Kittel[3].
11	EleNeg_Miedema	0.442	Electronegativity (in Volt) used in the Miedema model[6].
12	Heat_Capacity	0.042	Heat capacity at 298 K (in J/kg-mol.K)[7].
13	BoilingT	0.018	Boiling temperature (in K)[7].
14	Ion_Pot_3	0.004	The third ionization potentials to remove two electrons (in eV)[7].
15	NdUnfill	0.044	Number of unfilled *d* valence electrons.
16	NpVal	0.053	Number of *f* valence electrons.
17	Therm_Conduc	0.178	Thermal conductivity at 300 K (in W cm^{-1} K^{-1})[3,8].
18	WorkFunc	0.430	Work function of pure elements[9].
19	Heat_Sublimation	0.076	Heat of sublimation at 298 K (in J/mol)[7].
20	Ion_Pot_2	0.038	The second ionization potentials to remove two electrons (in eV)[7].
21	Number	0.032	Atomic number of pure elements in the periodic table.
22	Ele_Conduc	0.079	Electrical conductivity of metals in (ohm-cm)$^{-1}$ [3].
23	NUnfill	0.156	Number of total unfilled valence electrons.
24	Heat_Fusion	0.015	Heat of fusion at 298 K (in J/mol)[7].
25	V0_Miedema	0.047	Atomic volume (in cm^3/mol) used in the Miedema model[6]
26	Radius_Coval	0.282	Covalent radius (in pm) based on the collections of Wolfram Mathematica (WM); see "ElementData" in WM[5].
27	NsUnfill	0.155	Number of unfilled s valence electrons.
28	DebyeT	0.002	Debye temperature (in K) collected by Kittel[3].
29	Mass	0.030	Mass of pure elements.
30	Radius_vDW	0.094	Van der Waals atomic radius (in pm)[5,10].
31	EleDensity_Miedema	0.219	Electron density at the boundary of Wigner-Seitz cell used in the Miedema model[6].
32	G_wiki	0.152	Shear modulus (in GPa) of pure elements based on Wikipedia and Azom[11,12].

| 33 | Y_wiki | 0.165 | Young's modulus (in GPa) of pure elements based on Wikipedia and Azom [11,12]. |
34	No_Spectral_lines	0.017	Number of spectral lines of the elements [7].
35	NpUnfill	0.037	Number of unfilled p valence electrons.
36	EleNeg_Pauling	0.593	Electronegativity by Pauling scale (a dimensionless quantity) [5,10].
37	NfVal	0.009	Number of f valence electrons.
38	Ion_Pot_1	0.308	The first ionization potentials to remove one electron (in eV) [7]
39	Electron_Affinity	0.258	Electron affinity (in eV) [10].
40	B_wiki	0.275	Bulk modulus (in GPa) of pure elements based on Wikipedia and Azom [11,12]. Note that elastic properties of fcc Sr were taken from [13].
41	Nval	0.264	Number of total valence electrons.
42	MaxR_Ele_in_Solid	0.046	Maximum range of electrons in solid elements for electron energy of 15 keV (in mm) [7].
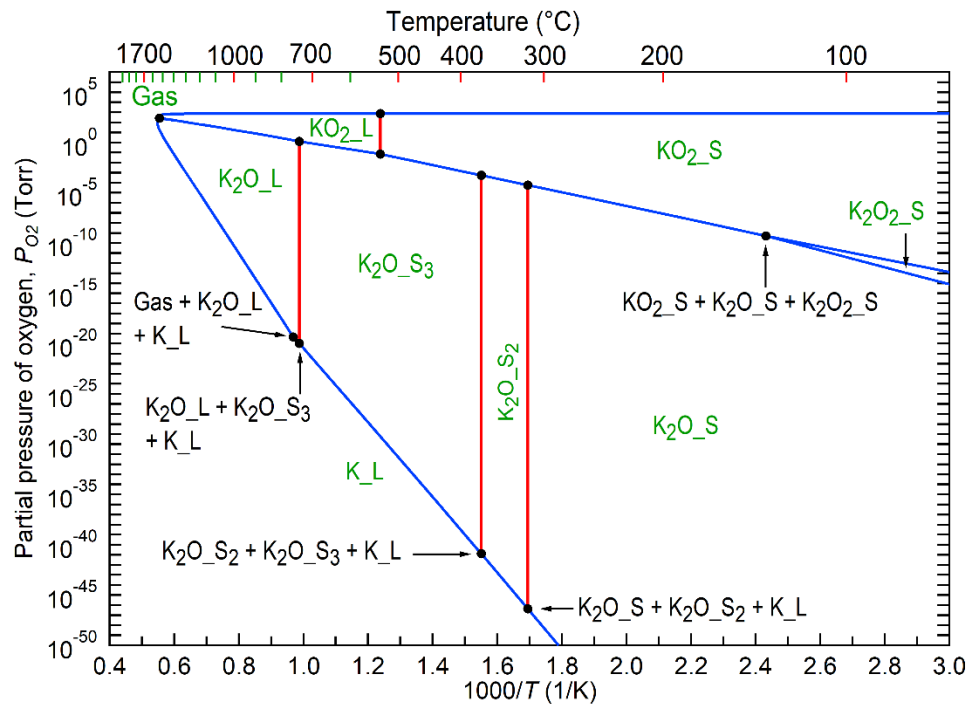
Figure S1. Calculated K-O pressure-temperature phase diagram in terms of the SSUB5 database (K_2O_2_S is stable below 411 K). With increasing temperature, the phase transitions follow K →

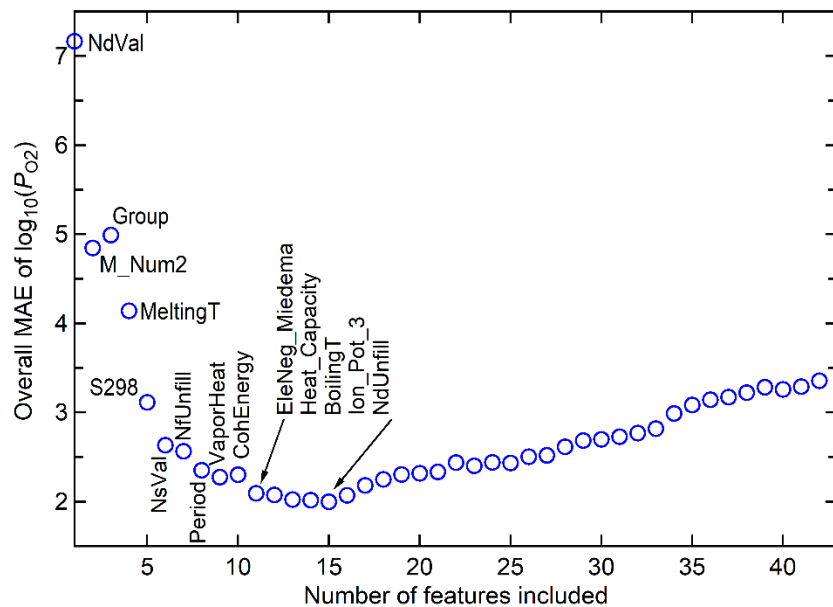K_2O → K_2O_2 (stable below 411 K) → KO_2 → Gas (O_2).

Figure S2. Examination of the combined features using the sequential feature selection method and the algorithm of Gaussian process regression (with the kernel function of matern52). Among the 42 features, the top 15 features are labeled in this figure.

References:

[1] X. Chong, S.-L. Shang, A.M. Krajewski, J.D. Shimanek, W. Du, Y. Wang, J. Feng, D. Shin, A.M. Beese, and Z.-K. Liu, "Correlation analysis of materials properties by machine learning: illustrated with stacking fault energy from first-principles calculations in dilute fcc-based alloys," J. Phys. Condens. Matter **33**(29), 295702 (2021).

[2] A. Zunger, "Systematization of the stable crystal structure of all AB-type binary compounds: A pseudopotential orbital-radii approach," Phys. Rev. B **22**(12), 5839–5872 (1980).

[3] C. Kittel, *Introduction to Solid State Physics* (John Wiley & Sons, Inc., Hoboken, NJ, 2005).

[4] A.T. Dinsdale, "SGTE data for pure elements," Calphad **15**(4), 317–425 (1991).

[5] "Wolfram Mathematica: Modern Technical Computing," https://www.wolfram.com/mathematica (accessed March 16, 2020).

[6] R.F. Zhang, S.H. Zhang, Z.J. He, J. Jing, and S.H. Sheng, "Miedema Calculator: A thermodynamic platform for predicting formation enthalpies of alloys within framework of Miedema's Theory," Comput. Phys. Commun. **209**, 58–69 (2016).

[7] G. V. Samsonov, *Handbook of the Physicochemical Properties of the Elements* (Springer, New York, 1968).

[8] "The Periodic Table", https://periodictable.com (accessed March 16, 2020).

[9] H.B. Michaelson, "The work function of the elements and its periodicity," J. Appl. Phys. **48**(11), 4729–4733 (1977).

[10] "Periodic Table of Elements - PubChem", https://pubchem.ncbi.nlm.nih.gov/periodic-table/ (accessed March 16, 2020).

[11] "Elastic properties of the elements (data page) - Wikipedia", https://en.wikipedia.org/wiki/Elastic_properties_of_the_elements_(data_page) (accessed March 16, 2020).

[12] "AZOM Materials", https://www.azom.com/ (accessed October 23, 2023).

[13] M.S. Anderson, C.A. Swenson, and D.T. Peterson, "Experimental equations of state for calcium, strontium, and barium metals to 20 kbar from 4 to 295 K," Phys. Rev. B **41**(6), 3329–3338 (1990).